ADVANCED MATERIALS TECHNOLOGIES
www.advmattechnol.de

Sliding Triboelectric Circular Motion Sensor with Real-Time Hardware Processing

Zhijie Xie, Zhenghui Zeng, Fei Yang, Jingliang Lv, Yu Wang, Rensuan Wu, Jiaxiu Liu, Zhong Lin Wang,* and Tinghai Cheng**

Since circular motion becomes an important part of automated circulation equipment, a sliding triboelectric circular motion sensor (S-TCMS) has been demonstrated to monitor the velocity and displacement of a circular motion. The S-TCMS consists of the stator and slider, which is integrated with automated circular motion equipment for sensing applications. When the slider of PTFE grid slides between the stator's electrodes, four electrical signals are produced in the staggered electrode. The experimental results show that the voltage amplitude remains constant at different sliding velocities, showing good sensing stability. Also, this work proposes a real-time hardware signal processing method, which converts the original S-TCMS signal into two standard square wave signals. The method makes the sensing detection of S-TCMS independent from electrostatic instrument and reduces the occupation of hardware resources. The sensing experimental results show that S-TCMS can detect the velocity of circular motion with the maximum velocity deviation rate of less than 0.37%, the angular position sensing detection accuracy of 0.42°. The S-TCMS shows good circular motion-sensing characteristics after hardware signal processing.

1. Introduction

With the rapid development of the electronic information industry, the fields of computers, communications, and consumer electronics have shown a great demand for the application of a circular motion platform for automated production line and assembly line.[1] In order to ensure product quality, mechanical motion of motion platforms requires accurate feedback on motion parameters from motion sensors.[2] In the past, with the high-speed development of photoelectric, magnetoelectric, capacitive, resistive, and other motion sensors, the main methods of the detection of circular motion have been the grating scale,[3,4] magnetic scale,[5] and hall sensor.[6] The research of the motion sensors, especially the linear motion sensor, has been very mature, but for a circular motion sensor, the existing technologies still face different limitations, including the low structure integration, high cost and complexity, and strict environmental requirements.

Recently, the triboelectric nanogenerator (TENG) proposed by Wang and his team has provided a new solution for circular motion sensing, which is based on Maxwell's displacement current theory.[7] When the external excitation is applied to a sensor, the TENG can sense sensitive mechanical motion and generate the electrical signal, whose characteristics can reflect the motion state.[8] In recent years, due to the sensing ability of the TENG, triboelectric sensors, including mechanical motion sensors,[9–12] gas sensors,[13–16] fluid sensor,[17] wearable sensor[18] and human-machine interface sensor[19] have been rapidly developed. In addition, many studies have demonstrated that TENG has advantages of wide material applicability, simple structure, small size, low cost, and high integration.[20–22] Meanwhile, Zhang et al. conducted in-depth study on improving the electrical output capacity of TENG.[23,24] Recently, many triboelectric mechanical motion sensors with a sliding freestanding triboelectric layer have been proposed for different detection objects, including linear motion sensors,[10,25] rotational motion sensors,[26,27] and angular motion sensors.[28,29] However, there is still a lack of research on the triboelectric motion sensor with circular motion as the object. Aiming at improving the angular displacement resolution of a freestanding triboelectric-layer-based motion sensor, a large number of studies have used the form of differential multi-electrode pairs, such as two and three pairs of electrodes.[10,30] Still, the multi-channel signal acquisition requires additional input interface resources, and direct detection of the sensed output signal relies on the equipment of electrostatic acquisition. At the same time, the method of

Z. Xie, J. Lv, Y. Wang, R. Wu
College of Mechanical and Electrical Engineering
Northeast Forestry University
Harbin 150042, China
E-mail: xiezhijie111@sina.com
Z. Zeng, F. Yang, J. Liu
School of Mechatronics Engineering
Harbin Institute of Technology
Harbin, Heilongjiang 150001, China
Z. L. Wang, T. Cheng
Beijing Institute of Nanoenergy and Nanosystems
Chinese Academy of Sciences
Beijing 101400, China
E-mail: zlwang@gatech.edu; chengtinghai@binn.cas.cn
Z. L. Wang, T. Cheng
CUSTech Institute
Wenzhou, Zhejiang 325024, China
Z. L. Wang
School of Materials Science and Engineering
Georgia Institute of Technology
Atlanta, GA 30332-0245, USA
The ORCID identification number(s) for the author(s) of this article can be found under https://doi.org/10.1002/admt.202100655.

DOI: 10.1002/admt.202100655

signal feature extraction applying PC software for signal processing on the original signal obtained from a sensor does not perform well for modularization and product application of the triboelectric motion sensor.

This work proposes a sliding triboelectric circular motion sensor (S-TCMS) that can be used to monitor the velocity and displacement of a circular motion and can be highly integrated into a circular motion platform. A fixed sheet of circular four-way staggered copper electrode is mounted into the circular motion platform orbit, which is used as a stator. The PTFE is processed into the grid pattern and secured to the bottom of the motion slider as a freestanding triboelectric layer. When the slider moves relative to the stator, the PTFE grid slides relative to the copper electrodes, thus causing the four-way staggered electrode to produce the electrical signal. The proposed sensor's output capability is experimentally tested, and the experimental results show that its signal amplitude remains constant at 6.8 V at different sliding velocities. In addition, this study introduces a real-time hardware signal processing method to convert the output signals of the triboelectric sensor into the standard two-channel differential square wave signals. By extracting the frequency and period number characteristics of square wave signals, the velocity and displacement of the circular motion sliding are detected. After hardware signal processing, the proposed S-TCMS can perform the sensing signal detection and standardization of sensing signal without the help of an electrostatic instrument, which is of great significance for the commercialization of triboelectric sensors. In terms of sensing characteristics, S-TCMS can detect the velocity of circular motion with the maximum velocity deviation rate of less than 0.37%. And the angular resolution of the S-TCMS reaches 0.375° with a displacement accuracy of 0.42° and a repeat positioning accuracy of 0.3°, which proves that the proposed sensor has a strong ability in angular displacement detection and repetitious stability.

2. Results and Discussion

2.1. Structural Design and Operating Principle

The proposed S-TCMS consists of a stator electrode unit and a slider unit, as shown in **Figure 1**a(i). The slider unit is driven by a servo motor to slide freely along the circular guide on a circular motion platform. The slider unit consists of an aluminum slider and a PTFE grid, as shown in Figure 1b. The

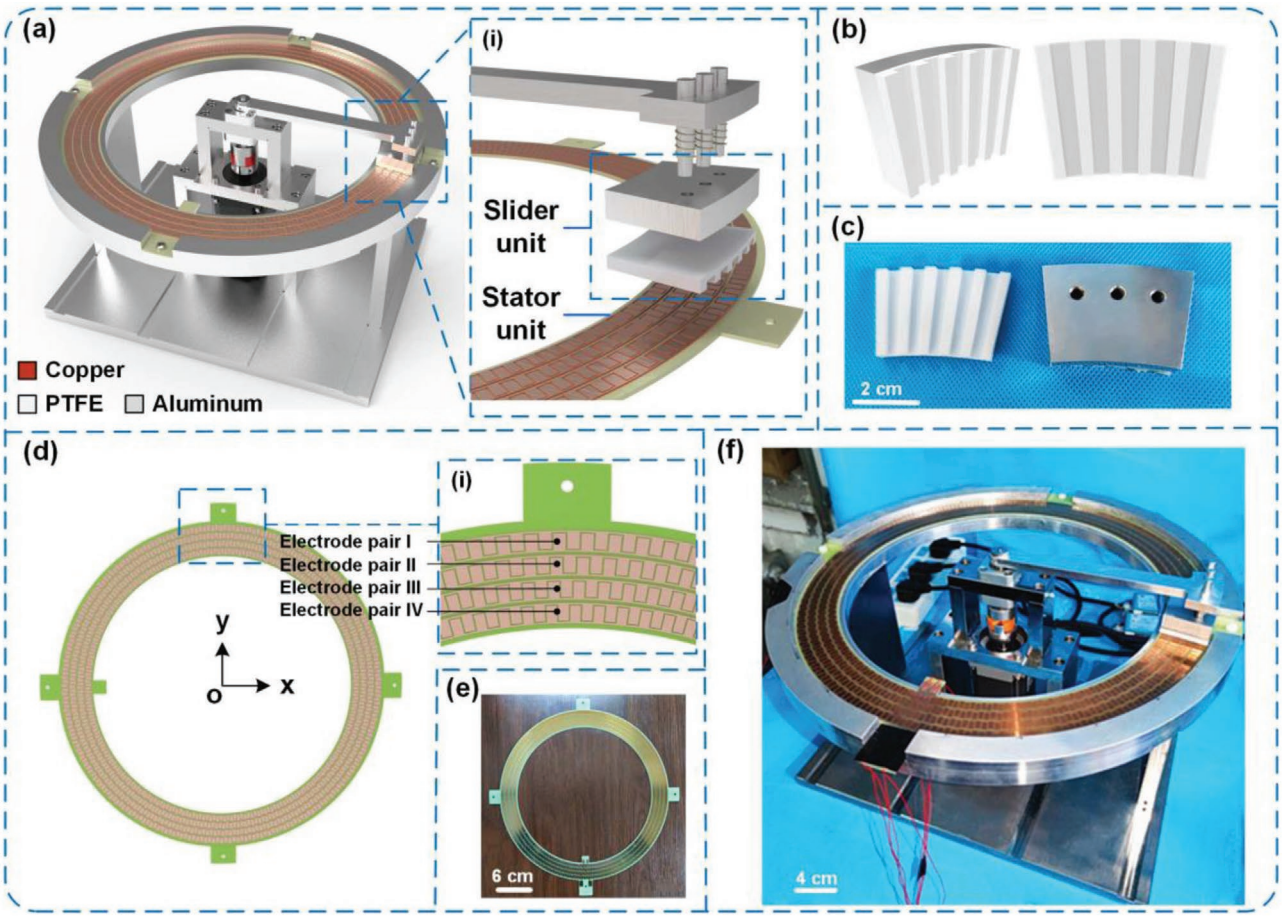

Figure 1. Structural design of the sliding triboelectric circular motion sensor (S-TCMS). a) Schematic structure of the S-TCMS, b) schematic structure of the slider and PTFE grid, c) photograph of the slider and PTFE grid, d) schematic structure of the four-way electrode, e) photograph of the four-way electrode, and f) photograph of the assembled S-TCMS.

aluminum slider is arranged with threaded holes for the purpose of connecting to the kinematic unit of the circular motion platform, and PTFE grid are adhered to the underside of the aluminum slider and used as a freestanding triboelectric layer of the S-TCMS. The structure of the fabricated slider unit is shown in Figure 1c. The slider is subjected to pressure perpendicular to the plane of motion by arranging a preloaded spring, so that the PTFE grid can adhere to the stator electrode surface well. When the slider unit moves, the PTFE grid slide against the stator electrode's upper surface. If a PTFE film is used, the PTFE surface will be broken and powdered after a long-time or high-speed movement due to the low hardness of the PTFE film. Therefore, this work adopts the PTFE grid in block solid structure with spring preload, which can adapt to the state of the platform surface's flatness using a preload so that it can better adhere to the copper electrode surface. Simultaneously, due to the thicker triboelectric layer of the PTFE solid of 2 mm compared to film, it can resist wear caused by friction for a long time (Figure S4, Supporting Information).

The stator unit is presented in Figure 1d, where it has a double-layer structure consisting of the copper electrode layer and rectangular glass epoxy substrate layer. The copper electrode layer is divided into four electrode pairs by fine grooves in the circular copper electrode. The electrode pairs are denoted as I, II, III, and IV and arranged adjacent to each other concentrically in the circular gyration radius direction, as shown in Figure 1d(i). The adjoining electrode pairs are staggered by one-eighth of a phase cycle in the circular gyration direction (Figure S1, Supporting Information). The sheet of electrode is in circular structures with inner and outer diameters of 150 and 190 mm, respectively, and a thickness of 3 mm. The fabricated stator unit of electrodes are arranged as shown in Figure 1e. The mounting and working methods of the slider and stator are described in more detail in the experimental section. The overall dimensions of the circular motion platform equipped with the S-TCMS are 420 mm (length) × 420 mm (width) × 38 mm (height), as shown in Figure 1f.

The S-TCMS uses PTFE and copper as triboelectric layer materials, which have opposite electronegativity. The copper electrode not only acts as an electrode but also participates in the triboelectrification process. The working principle of the S-TCMS is illustrated in **Figure 2**a. Taking a single electrode pair as an example, the PTFE grid acts as an electronegative freestanding triboelectric layer, while the copper electrode acts as a conductive layer and an electropositive triboelectric layer. When the stator moves, the PTFE surface will accumulate equal but opposite triboelectric charges generated by the friction of two copper electrodes, and the separation contact of the freestanding triboelectric layer alternating on the electrode will be divided into four states.

In the first state shown in Figure 2a(i), the PTFE grid is aligned with the copper electrode A. According to the electrostatic induction effect, the positive and negative charges on the PTFE grid and the copper electrode consist of equal quantities of positive and negative charges on their surfaces and are in the electrostatic equilibrium state, wherein no induced potential is generated in the external circuit that is placed between the copper electrodes A and B. When the PTFE grid performs a circular motion, it gradually changes from the first to the second state, as shown in Figure 2a(ii). During this motion, due to the electrostatic induction, the positive charge on the electrode A will gradually transfer to electrode B, thus forming a transient current in the external circuit. When the PTFE grid has the same electrostatic induction area as the two electrodes, its outward current reaches its maximum value. When the PTFE grid continues to move until it completely overlaps with the copper electrode B, it will enter the third state, as shown in Figure 2a(iii), wherein all the positive charges that were originally on the electrode A will be transferred to the electrode B due to the electrostatic induction, and then returns to the electrostatic equilibrium state. As shown in Figure 2a(iv), when the PTFE grid continues to move, the positive charges on the electrode B flow back to the electrode A, which generates a reverse current in the external circuit. Finally, the PTFE grid returns to the first state, thus completing a full-motion cycle. Potential differences are generated between the two electrodes due to the different positions of the freestanding triboelectric layer. Therefore, when a load is connected externally, the free electrons in the external circuit will be driven by the potential difference to generate a flow. Besides, when the freestanding triboelectric layer moves periodically back and forth between the two electrodes, a regularly changing output electrical signal is generated.

When the PTFE grid is sliding, the bottom of the PTFE grid is rubbed with four electrode pairs simultaneously, as shown in Figure 2b. Phase A, B, C, and D correspond to the working state of the slider at electrode pair I, II, III, and IV, respectively. When the PTFE grid overlaps completely with the area of electrode A of electrode pair I, PTFE grid overlaps 3/4 of the area of electrode A and 1/4 of the area of electrode B of electrode pair II; In the case of electrode pair III, the PTFE grid strip overlaps 1/2 of the areas of electrodes A and B. In electrode pair IV, the PTFE grid strip overlaps 1/4 of the area of electrode A and 3/4 of the area of electrode B. Thus, the adjacent phases differ from each other by 1/8 motion period, and the theoretical phase relationship of S-TCMS is shown in Figure 2c.

The COMSOL multi-physics simulation software was used to verify the feasibility of the proposed principle. In the open-circuit state, the potential distribution of units of electrodes A and B was simulated. After sliding friction, the copper electrode had a positive charge, while the PTFE grid surface had a negative charge. The potential distribution curves of electrodes A and B at different positions of the PTFE grid state are presented in Figure 2d. Based on the obtained results, the potential difference between the two electrode gradually increased as the PTFE grid slid, thus verifying that the difference of potential can drive the current flow in the external circuit between the electrodes and generate an electrical output signal.

2.2. Output Characteristics

Obtaining the electrical output's characteristics is the basis of performance testing of the S-TCMS. To test the electrical performance of the S-TCMS, an electrostatic meter (Keithley 6514) was used to study the voltage and current of the S-TCMS. The

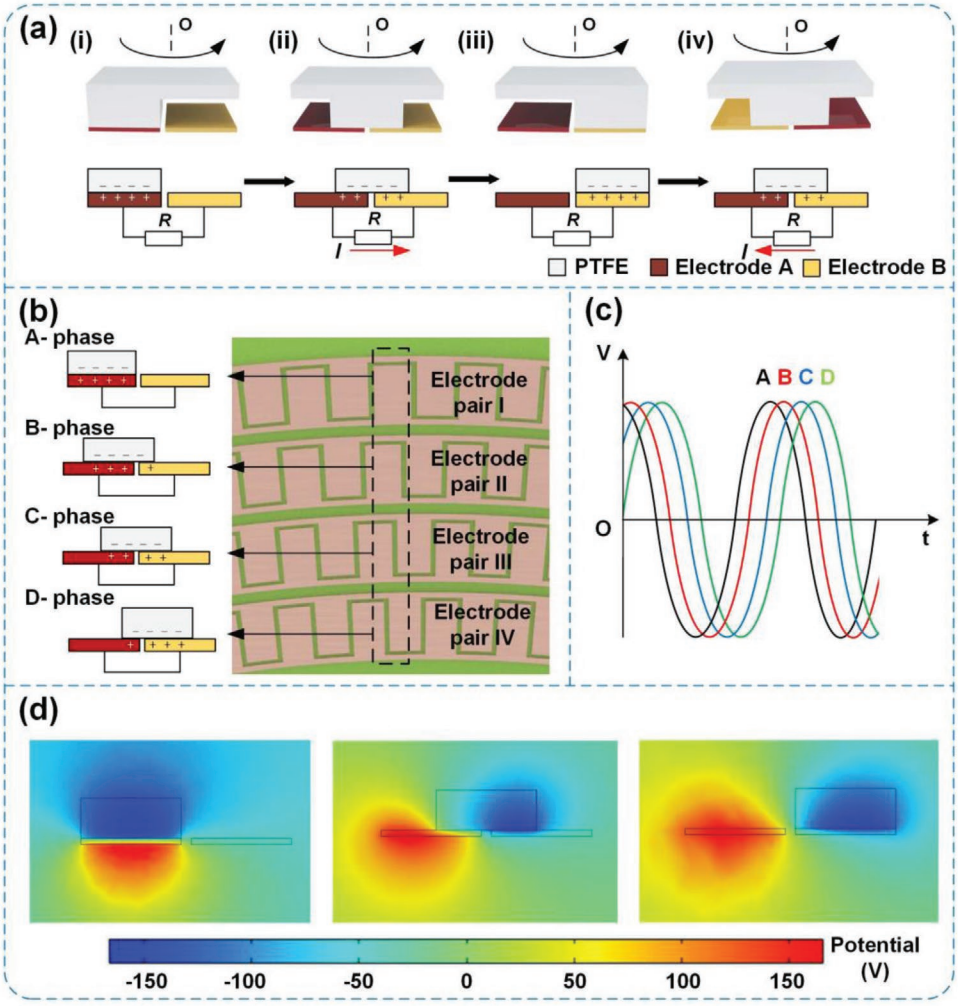

Figure 2. Operation principle of the S-TCMS. a) Schematic of the operation principle of the S-TCMS, b) characteristic of the electrode pair phase arrangement, c) voltage signal waveform of the electrode pair phase arrangement, and d) potential distributions of the S-TCMS in three different states simulated using COMSOL.

regular operation of the S-TCMS needs to be within the operating velocity range of the circular motion platform, so in the test, the velocity range of the test S-TCMS was in the range from 30 to 200 mm s^{-1}, which was selected according to the common working velocity ranges of motion platforms. The motion velocities of the servo motor were set to 10, 20, 30, 40, 50, 60, and 70 rpm, which corresponded to the linear velocities test points of 30.4, 60.7, 91.1, 121.5, 151.8, 182.2, and 212.6 mm s^{-1}, respectively. Following the theory of a freestanding triboelectric-layer-based nanogenerator,[21] the open-circuit voltage was expressed as:

$$V_{OC} = \frac{2\sigma x(t)}{\varepsilon_0} \tag{1}$$

where σ denotes the surface charge density, ε_0 is the dielectric constant in the vacuum, and $x(t)$ is the sliding distance of the slider in a cycle. The open-circuit voltage of the freestanding triboelectric-layer-based nanogenerator was proportional to the surface charge density and independent of the slider motion velocity. So, as shown in **Figure 3**a, the open-circuit voltage amplitude of S-TCMS was stable at ≈6.8 V under different operating rates.

From the theory for a freestanding triboelectric-layer-based nanogenerator,[22] the short-circuit current is expressed as

$$I_{SC} = \frac{Q_{SC}}{\Delta t} \tag{2}$$

where Q_{SC} denotes the short-circuit charge transferred, and Δt is the rate of charge transfer. From Equation (2), the amplitude of the short-circuit current increases with increasing velocity, which is consistent with the short-circuit current test results of the S-TCMS, which are presented in Figure 3b. The effect of the S-TCMS on the output current signal under different external loads was also investigated. As shown in Figure 3c, when the external load value was small (less than 0.1 MΩ), the output current of the S-TCMS was close to the short-circuit current because of the high internal resistance of the S-TCMS. When the external resistance increased from 1 to 100 MΩ, the

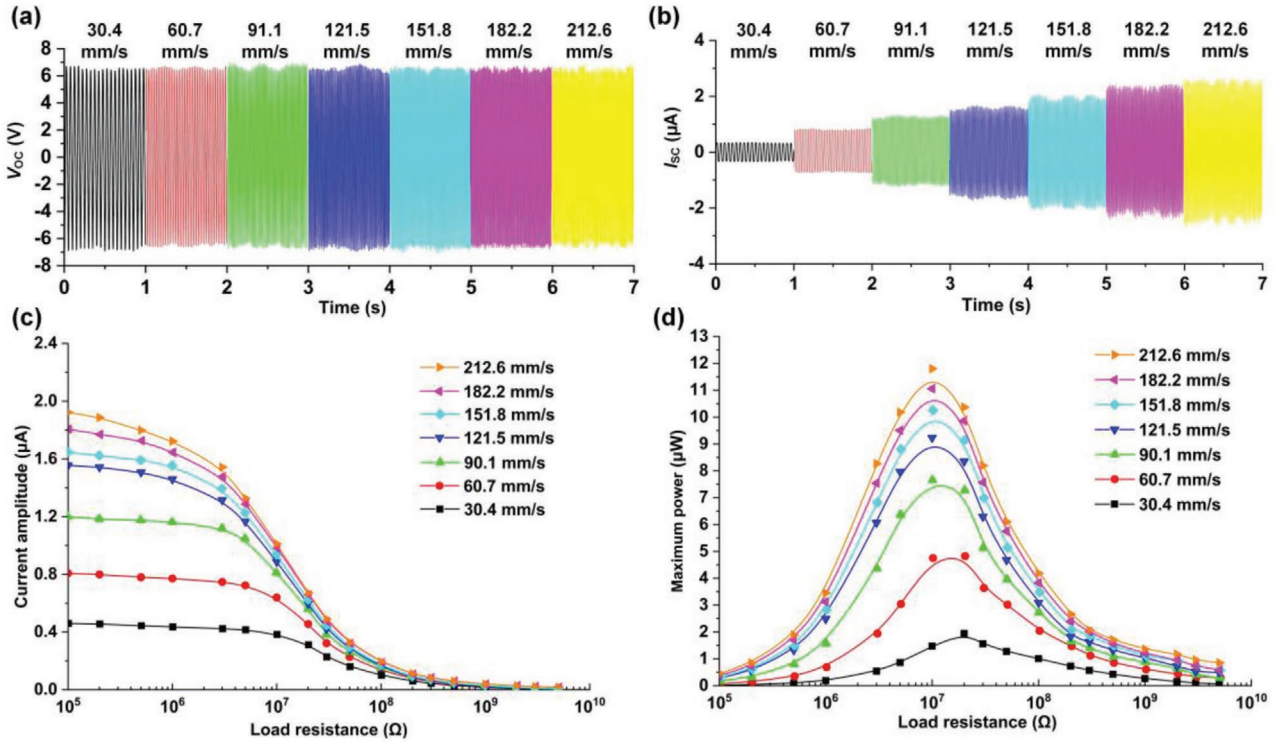

Figure 3. Characteristics of the S-TCMS. a) Open-circuit voltage (V_{OC}), b) short-circuit current (I_{SC}) of A-phase for different sliding velocities, c) short-circuit current across various external resistances, and d) output maximum power across various external resistances.

external current decreased substantially. As the resistance continued to increase, the external resistance was much larger than the internal resistance of the S-TCMS, and the current of the external circuit gradually decreased to zero. The points of change in trend of the resistance-current curves differed under different operating velocities; thus, different sliding velocities affected the internal resistance of the S-TCMS. To illustrate the change in the internal resistance more intuitively, the output power curves were analyzed under different sliding velocities. According to

$$P_m = I_m^2 R \tag{3}$$

where I_m denotes the maximum instantaneous current, R is the external load, and P_m is the maximum instantaneous power. As shown in Figure 3d, the maximum output power-external resistance curves of the S-TCMS were tested under different operating velocities. When the external resistance of the S-TCMS was much smaller or larger than its internal resistance, the maximum output power of its external circuit was low. In contrast, when the external resistance of the S-TCMS was close or equal to its internal resistance, the external circuit reached the maximum output power. Therefore, the internal resistance of the S-TCMS changed as the sliding velocity increased. At a sliding velocity of 30.4 mm s^{-1}, the internal resistance was ≈20 MΩ, and when the sliding velocity increased to 212.6 mm s^{-1}, the internal resistance of the S-TCMS was ≈9 MΩ. The experimental results show the electrical characteristics of the S-TCMS, which coincide well with the subsequent signal processing and sensing test results.

2.3. Signal Processing

The TENG has excellent sensing potential, but due to its unique electrical characteristics, it often requires using specific equipment, such as an electrometer for signal acquisition, which limits its practical, commercial application. To address this limitation, this paper proposes a real-time hardware signal processing method of the S-TCMS based on the electrical characteristics and signal features.

Analysis of the electrical characteristics of the S-TCMS has revealed that improving the Angular displacement resolution of the S-TCMS requires increasing the number of grid cycles of the entire circular electrode by reducing the angle occupied by a motion period. However, as a narrower width of a single finger electrode of the S-TCMS will lead to a lower friction area, the voltage and current of the S-TCMS will reduce. The low amplitude and poor stability of the voltage signal of the sensor will affect the speed and the accuracy of sensing in software signal processing. Therefore, this work introduces a real-time hardware-based method for processing the original signal of the S-TCMS; the overall steps of signal processing are shown in **Figure 4**. First, the operational amplifier module LM324 chip is used for DC filtering and amplification of the original signal, as shown in Figure 4b(i). The voltage signal of the S-TCMS (with the load R_0 = 10 MΩ) is input into the first-stage DC filter circuit to eliminate the DC bias in the original voltage signal and to perform noise filtering. After that, the filtered S-TCMS signal is input into the next stage LM324 operational amplifier for the purpose of amplifying the voltage signal with the amplitude of 4.2 V by five times, thus obtaining the trapezoidal wave

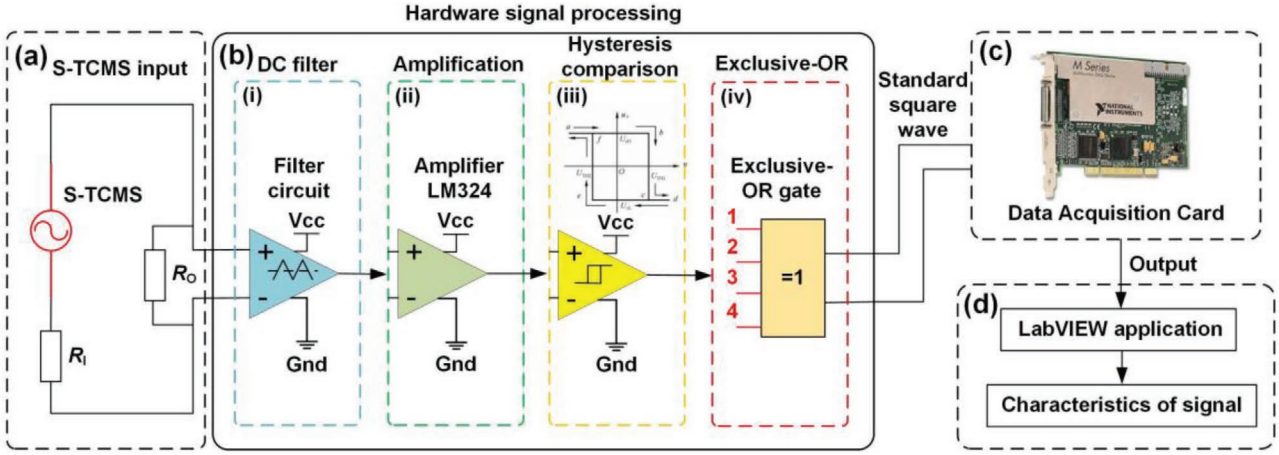

Figure 4. Signal flow process. a) The original input signal circuit of the S-TCMS, b) hardware signal processing method of S-TCMS, c) data acquisition method of the S-TCMS, and d) extraction of sensing signal features by PC.

voltage signal, as shown in Figure 4b(ii). The magnification of the operational amplification module can be adjusted according to the amplitude of the original signal input by S-TCMS, so that the consistency of the trapezoidal wave shape of the amplified four-way signal is guaranteed. To ensure the sensed signal's phase accuracy, the trapezoidal waveform signal is fed to the hysteresis comparison module, as presented in Figure 4b(iii), which converts the trapezoidal waveform signal into a square waveform signal with a duty ratio of 1:1. The Exclusive-OR gate circuit and experimental results are shown in Figure S2 (Supporting Information). Finally, the four standard square wave signals with a phase difference are fed to the Exclusive-OR gate and synthesized into the standard two square wave signals with a phase difference of $\pi/2$, which are commonly used in motion sensors in the industry, as displayed in Figure 4b(iv). After the S-TCMS hardware signal processing, the standard sensing signals can be acquired directly via the data acquisition card (NI PCI-6259), as shown in Figure 4c. For the four signals of S-TCMS, only two ports of the acquisition card need to be occupied. The number and frequency of upper and lower edges of two digital signals are extracted and calculated by the LabVIEW software, as shown in Figure 4d, thus, realizing the detection of the circular motion velocity and position of the S-TCMS. Due to the reliability of the hardware analog circuit with a high transmission rate, the stability and timeliness of hardware signal processing were better than those of the existing software signal feature extraction methods for the triboelectric sensor. Hence, the proposed method can overcome the application limitations of the S-TCMS in terms of detection means and can be extended to freestanding triboelectric-layer-based motion sensors for better production performance.

To verify the feasibility of hardware signal processing, the S-TCMS slider was operated at a linear velocity of 91.1 mm s^{-1} (30 rpm), and an oscilloscope was used to test the signal transmission status in real-time during the hardware processing (Figure S3, Supporting Information). The four original voltage signals of the S-TCMS open circuit (**Figure 5**a) corresponded to phases A, B, C, and D. The original signals have noise and DC bias and differ by $\pi/4$ in phase between each path but had the same frequency of 60 Hz. The original signal was fed to the two-stage operational amplifier for DC filtering and amplification, and the amplifier module was connected to a voltage of ±4.5 V, so the minimum and maximum output voltage of the op-amp module were −4.5 and 4.5 V, respectively. According to the original signal amplitude, the amplification is set to five times. The triangular waveform was converted into a trapezoidal waveform during the amplification process, and its phase and frequency characteristics remained unchanged, as shown in Figure 5b. After that, the trapezoidal waveform was fed to the hysteresis comparison circuit, and the upper and lower limits of the voltage jump were taken as +2.42/−2.71 V; more information about the hysteresis comparison is given in Figure S2, Supporting Information. The amplitude of the converted square wave with different phases was ±4.5 V, as presented in Figure 5c. The video demonstration is given in Video S1 (Supporting Information).

The zero-value voltage comparator was used to return the output signal with the negative square wave amplitude to zero by setting the comparison voltage to 0 V, thus transforming the voltage analog signal to the digital signal, as shown in Figure 5d. The phase, frequency, and number of periods in the digital signal remain the same as in the original signal. Since the S-TCMS outputted four-way signals, if the four signals were acquired simultaneously, it would both occupy an additional hardware interface and reduce the application capability of the S-TCMS. Therefore, phases A and C (phases B and D) of the four signals were synthesized into a single square wave signal with a double frequency by the Exclusive-OR function, as shown in Figure 5e, which reduced the number of passes to the acquisition card. The square wave signal synthesized by phases A and C was denoted as phase M, and the square wave signal synthesized by phases B and D was denoted as phase N. The frequency of phases M and N was the same, and it was 120 Hz, and their phase difference was $\pi/2$, which was the output signal of a standard industrial velocity-position sensor, as shown in Figure 5f. After using the four-way staggered electrode, the angular displacement resolution of the sensor is four times higher than that of the single electrode, reaching 0.375°.

In addition to the case of combining four signals into two signals, the proposed method can be extended to multiple

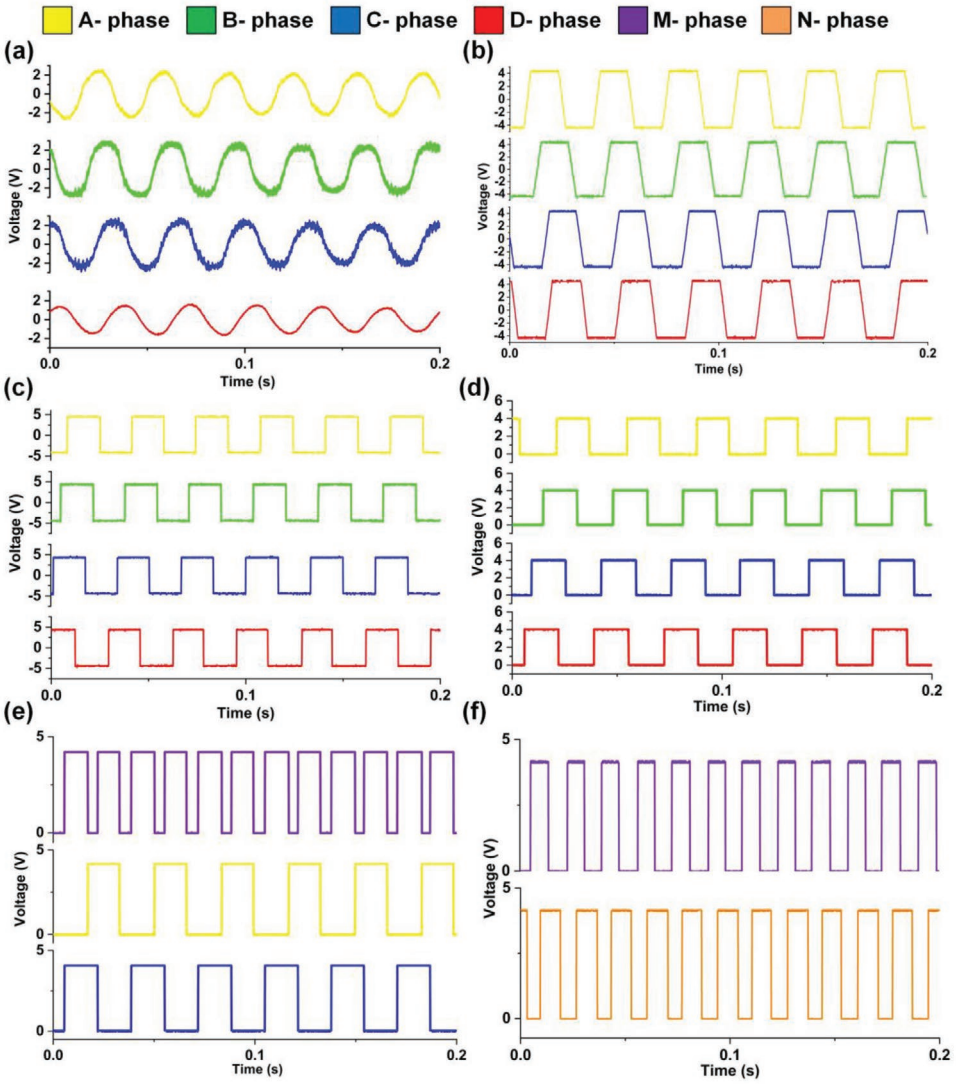

Figure 5. Experimental results of hardware signal processing. a) The original input signal circuit of the S-TCMS (the velocity of the slider is 91.1 mm s^{-1}, load 10 MΩ), b) signal of S-TCMS after DC filtering and operational amplification, c) signal of S-TCMS after hysteretic comparison, d) signal of S-TCMS after the zero comparison, e) signal of S-TCMS after the XOR comparison, and f) the output signal of S-TCMS after hardware signal processing.

differential applications, which can effectively reduce the requirement for hardware resources. The frequency characteristics of the output standard square wave signal and the number of edge jumps can reflect the velocity and displacement information of the slider.

3. Circular Platform and Sensing Application

For realizing the circular motion sensing detection of the S-TCMS, the S-TCMS was applied to the circular motion platform. The circular motion platform was mainly divided into two parts, the top part and the bottom part. The top part mainly consisted of the drive arm, drive shaft, connecting rod, and the S-TCMS slider unit, as shown in **Figure 6**a; the bottom part mainly included the servo motor, code plate, base, coupling, and the motion platform, wherein the sheet of the electrode was installed, as shown in Figure 6b. The servo motor, which was connected to the drive shaft via coupling, was fixed to the base. The drive shaft kept the drive arm synchronized with the drive shaft through a nut. The end of the drive arm was arranged with three mounting hole slots to connect with rods, and the connecting rods were fixedly connected to the slider unit through threads. And the slider, which could move in a direction perpendicular to the platform surface relative to the drive arm, could be pressed on the platform surface through spring. When the servo motor rotated, the shaft drove the arm and the motion unit to rotate around the motor axis together. The motor shaft coincided with the axis of the circular platform, so the slider could maintain the same angular velocity and angular displacement as the servo motor in a circular motion on the circular platform. Circular motion control of the slider could be achieved by controlling the motion of the servo motor, including different motion velocities, forward and reverse rotation, and positioning operation.

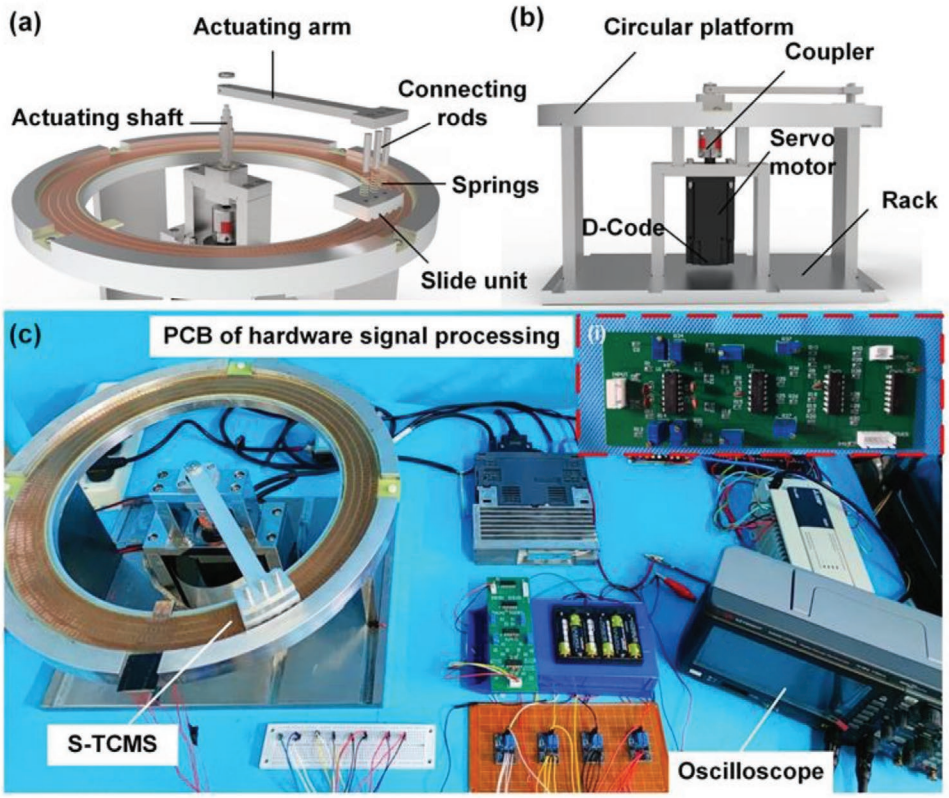

Figure 6. Circular motion platform with the S-TCMS. a) The top structure of the circular motion platform, b) the bottom structure of the circular motion platform, and c) photograph of the test system.

A circular motion-sensing experiment platform was built, as shown in Figure 6c. The S-TCMS was well integrated into the circular motion platform, and the servo motor was controlled by a special servo amplifier. As presented in Figure 6c, the printed circuit board (PCB) board of the hardware processing circuit was built and connected to the output signal of the S-TCMS, and the output digital signal of the PCB board was connected to the data acquisition card port, and the oscilloscope was used for real-time monitoring of the output sensing signal to ensure the output signal's reliability. The waveform of the experimentally detected sensing signal is shown in Figure S4 (Supporting Information).

To extract the signal characteristics of the digital square wave signal, the LabVIEW sensing acquisition system was used to realize the acquisition of the frequency and upper and lower edge jumps of a square wave signal, as shown in **Figure 7**a. The real-time velocity and displacement of the slider could be obtained by detecting the frequency, and the sum of edge jumps of the square wave input signal in real-time. Video demonstrations are given in Videos S2 and S3 (Supporting Information).

The sensing characteristics of the S-TCMS were investigated by means of a sensing test system. First, the linearity of the velocity detection of the S-TCMS was tested, and the results showed that the angular velocity detected by the S-TCMS had high linearity with the angular velocity detected by the high-precision code plate of the servo motor (4,200,000 pulses per revolution), as presented in Figure 7b. The maximum velocity deviation rate was less than 0.37% in the interval of working velocity, as shown in Figure 7c. The obtained results indicated that the S-TCMS had good circular velocity detection capability that could meet the accuracy requirements of industrial velocity sensors. To evaluate the detection of circular displacement, the sensing test was conducted, and the adopted calculation method was the cumulative summation of the numbers of edge jumps of the two square waves. Based on the results, the S-TCMS could generate 960 edge jumps during one circle of the slider movement, achieving the angular resolution of 0.375°, as shown in Figure 7e. In Figure 7e, the linear relationship between the angular position detected by the S-TCMS and the angular position of the servo motor code plate is displayed. Figure 7d shows the angular position deviations at different angular positions. The maximum angular position deviation of the one-circle motion was 0.420°. The repetition accuracy of the angular position detection of the S-TCMS was also tested, and results are shown in Figure 7f,g. The experiments were conducted at 15° intervals, and the repetition accuracy of the S-TCMS at each position was tested separately. The length of the interval of repeated positioning error was less than 0.3° at different angle positions. Hence, the S-TCMS has the capability of motion sensing.

4. Conclusion

This paper proposes an S-TCMS that can achieve circular motion detection in real-time under large-radius circular

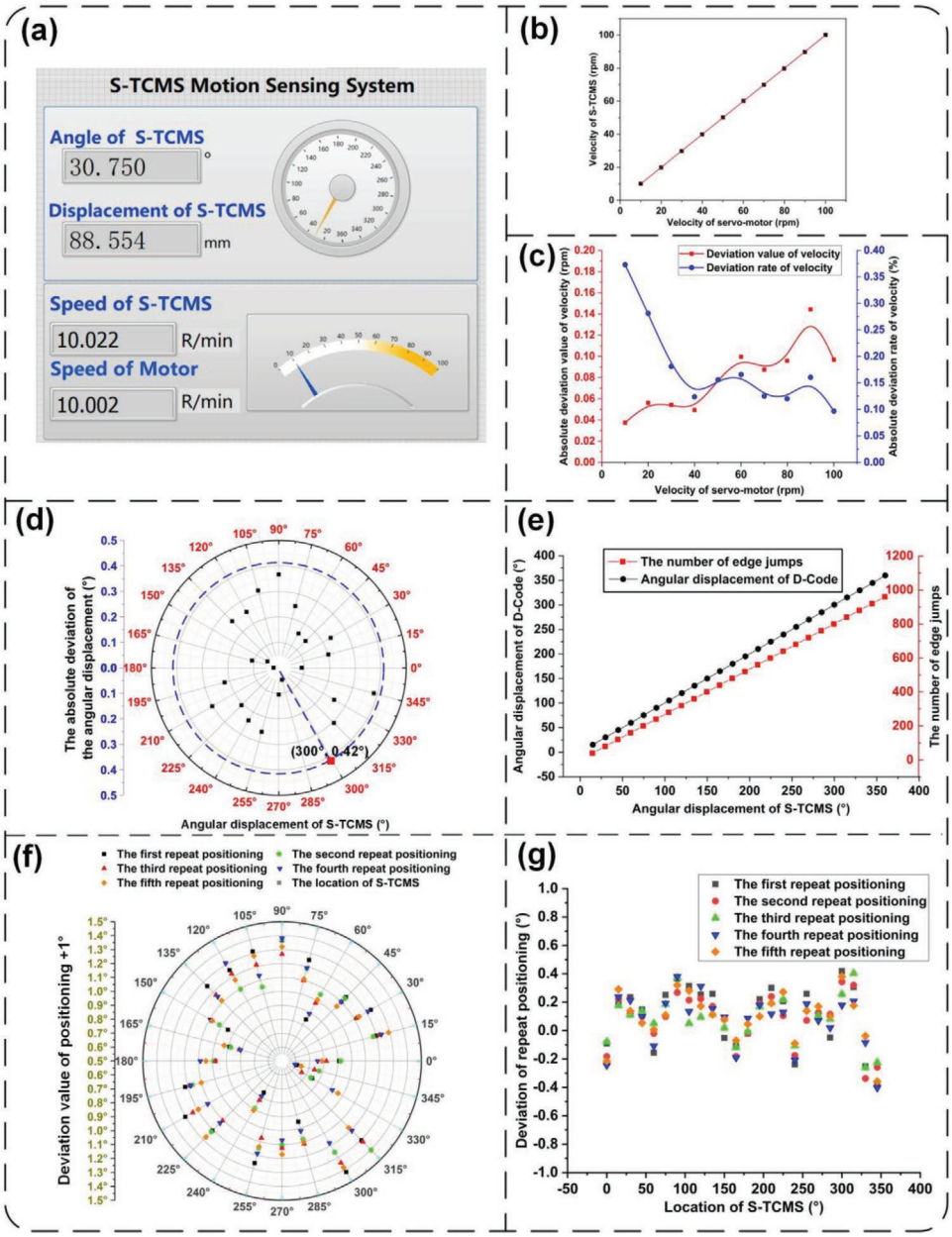

Figure 7. Test of S-TCMS sensing performance. a) LabVIEW sensor test system, b) linear relationship of velocity between S-TCMS and servo motor, c) deviation value and deviation rate of velocity between S-TCMS and servo motor, d) the angular displacement deviation between servo motor and S-TCMS, e) linear relationship of angle displacement between servo motor and S-TCMS, f,g) the repeat accuracy of the angular displacement of S-TCMS at different angle positions.

displacement trajectories by applying the operating mode of freestanding triboelectric-layer-based nanogenerators. The S-TCMS consists of the slider and stator units. The slider unit has a PTFE grid attached to its bottom, while the stator unit is a sheet of four-way staggered circular electrode. The angular displacement resolution of the four-way staggered circular electrode is four times that of a single electrode pair. The electrical characteristics and signal features of the proposed S-TCMS are determined and analyzed. In addition, a real-time hardware signal processing method for the original output of the S-TCMS is proposed. After the PCB circuit processing, the signal is transformed into a standard two-way square wave signal so that the S-TCMS sensing signal can be directly acquired by the data acquisition card in real-time. This method can effectively reduce the dependence of the four-way electrode on the number of ports of the data acquisition card and improve the S-TCMS application capabilities in signal acquisition when triboelectric sensors are used in practice. The experimental results show that the proposed S-TCMS has good linearity in sensing detection, and the detected signal frequency can reflect the velocity of the slider since the maximum velocity deviation rate is less than 0.37%. Meanwhile, the angular displacement resolution of

0.375° and the displacement accuracy of 0.42° is achieved, and the length of the interval of repeated positioning error was less than 0.3°. Therefore, S-TCMS can sense the slider motion on a circular motion platform well and with high stability.

5. Experimental Section

Fabrication of the S-TCMS and Hardware Processing Circuit: The S-TCMS consisted of an aluminum alloy slider, a PTFE grid, and a sheet of circular copper electrode. The aluminum alloy slider had a threaded hole for connection to the moving parts; the PTFE grid was cut from the PTFE sheet with a grid width of 1.3° and a pitch of 1.7°; the inner and outer diameters, angle, and thickness of the sector sheet were 300 mm, 376 mm, 16.5°, and 2 mm, respectively. The sheet of the electrode was composed of four concentric circular staggered electrode pairs. The finger-width of a single electrode was 1.3°, and the slit width between the staggered electrode was 0.2°. The specific style and size of the staggered electrode are presented in Figure S1 (Supporting Information). The electrode was fabricated using the industrial PCB double-layer board technology, etched in the staggered electrode style, with a copper thickness of 2.1 mil, and encapsulated on a 1.6-mm-thick circuit board substrate; the middle two electrodes led to the lower board, and the outer two electrodes led to the upper board. The circuit board substrate was evenly arranged with four through-holes for mounting the sheet of electrode on the guide of the circular motion platform.

The real-time hardware processing circuit used two LM324 chips to build the DC filter and amplifier module, LM339 chips to build the hysteresis comparison module, and 74LS138 Exclusive-OR gate chips to perform Exclusive-OR processing. The electrode was made by the industrial PCB technology with the power ground and input and output ports.

Measurement: The S-TCMS was assembled on a circular motion positioning platform, and the drive servo motor used in the platform with the code plate (Mr-J4, Mitsubishi, Japan) was connected to the aluminum alloy drive arm via coupling to drive the slider movement. The experiment was conducted in the clean laboratory environment with temperature of 23 °C and humidity of 42%. The electrical characteristics of the S-TCMS were measured using an electrometer (6514, Keithley, USA), and the signal state was monitored using an oscilloscope (DSOX1204A, KEYSIGHT, China). The original signal was fed to the PCB board for hardware signal processing, and then the output signal after signal processing was fed to a data acquisition card (PCI-6259, National Instruments, USA), and finally, input to the computer. The sensing test system was designed using the LabVIEW software platform to realize real-time data acquisition control and analysis.

Supporting Information

Supporting Information is available from the Wiley Online Library or from the author.

Acknowledgements

Z.X., Z.Z., and F.Y. contributed equally to this work. The authors are grateful for financial support from the National Natural Science Foundation of China (Grant number 51805109) and the Natural fund project of Heilongjiang Province (Grant number TD2020C001).

Conflict of Interest

The authors declare no conflict of interest.

Data Availability Statement

The data that support the findings of this study are available from the corresponding author upon reasonable request.

Keywords

circular motion, four-way staggered electrode, PTFE grid, real-time hardware signal processing, triboelectric motion sensor

Received: June 1, 2021
Revised: July 13, 2021
Published online:

[1] I. O. Yilmaz, H. O. Gunther, S. Jain, *Int. J. Adv. Manuf. Technol.* **2009**, *42*, 335.
[2] T. Klopot, G. Polakow, I. Parysz. *2016 21st Int. Conf. on Methods and Models in Automation and Robotics (Mmar)*, **2016**, pp. 140–145.
[3] Y. Wang, H. Y. Chen, Z. K. Liu, Y. L. Hong, *Opt. Eng.* **2016**, *55*, 107103.
[4] X. Xiao, Y. Kang, Z. Hou, W. Qiu, X. Li, X. Li, *Exp. Mech.* **2010**, *50*, 239.
[5] P. Y. Song, J. Y. Zhang, M. Li, S. Wang, *Appl. Mech. Mater.*, **2013**, *300–301*, pp. 1579–1583.
[6] T. Q. Hung, F. Terki, S. Kamara, K. Kim, S. Charar, C. Kim, *J. Appl. Phys.* **2015**, *117*, 154505.
[7] Z. L. Wang, *Mater. Today* **2017**, *20*, 74.
[8] F. R. Fan, Z. Q. Tian, Z. L. Wang, *Nano Energy* **2012**, *1*, 328.
[9] Z. Xie, J. Dong, Y. Li, L. Gu, B. Song, T. Cheng, Z. L. Wang, *Extreme Mech. Lett.* **2020**, *34*, 100595.
[10] Z. Xie, J. Dong, F. Yang, R. Xu, Q. Gao, T. Cheng, Z. L. Wang, *Extreme Mech. Lett.* **2020**, *37*, 100713.
[11] B. Zhang, Z. Wu, Z. Lin, H. Guo, F Chun, W. Yang, Z. L. Wang, *Mater. Today* **2021**, *43*, 37
[12] J. Zhao, J. Mu, H. Cui, W. He, L. Zhang, J. He, X Gao, Z. Li, X. Hou, X. Chou, *Adv. Mater. Technol.* **2021**, *6*, 2001022.
[13] D. Wang, D. Zhang, Y. Yang, Q. Mi, J. Zhang, L. Yu, *ACS Nano* **2021**, *15*, 2911
[14] D. Zhang, Z. Xu, Z. Yang, X. Song, *Nano Energy* **2020**, *67*, 104251.
[15] D. Zhang, Y. Yang, P. Li, M. Pang, Q Xue, *Nano Energy* **2019**, *65*, 103974.
[16] D. Zhang, D. Wang, Z. Xu, X. Zhang, Y. Yang, J. Guo, B. Zhang, W. Zhao, *Coord. Chem. Rev.* **2021**, *427*, 213597.
[17] J. Chen, H. Y. Guo, J. G. Zheng, Y. Z. Huang, G. L. Liu, C. G. Hu, Z. L. Wang, *ACS Nano* **2016**, *10*, 8104.
[18] X. J. Pu, H. Y. Guo, Q. Tang, J. Chen, L. Feng, G. L. Liu, X. Wang, Y. Xi, C. G. Hu, Z. L. Wang, *Nano Energy* **2018**, *54*, 453.
[19] Q. He, Y. F. Wu, Z. P. Feng, C. C. Sun, W. J. Fan, Z. H. Zhou, K. Y. Meng, E. D. Fan, J. Yang, *Nano Energy* **2019**, *59*, 689.
[20] Z. Wang, Y. Yu, Y. T. Wang, X. H. Lu, T. H. Cheng, G. Bao, Z. L. Wang, *ACS Nano* **2020**, *14*, 5981.
[21] Z. Y. Wu, T. H. Cheng, Z. L. Wang, *Sensors-Basel* **2020**, *20*, 2925.
[22] Z. L. Wang, J. Chen, L. Lin, *Energy Environ. Sci.* **2015**, *8*, 2250.
[23] B. Zhang, F. Chun, G Chen, T. Yang, A. Libanori, K. Chen, G. Conta, D. Xiong, C. Yan, W. Yang, J. Chen, *Cell Rep. Phys. Sci.* **2021**, *2*, 100441.
[24] B. Zhang, G. Tian, D. Xiong, T. Yang, F. Chun, S. Zhong, Z. Lin, W Li, W. Yang, *Research* **2021**, *2021*, 7189376.
[25] X. Yin, D. Liu, L. Zhou, X. Li, G. Xu, L. Liu, S. Li, C. Zhang, J. Wang, Z. L. Wang, *Adv. Funct. Mater.* **2020**, *30*, 2002547.
[26] D. Kim, I.-W. Tcho, Y.-K. Choi, *Nano Energy* **2018**, *52*, 256.

[27] S. Lin, L. Zhu, Y. Qiu, Z. Jiang, Y. Wang, J. Zhu, H. Wu, *Nano Energy* **2021**, *83*, 105857.
[28] Y. Wu, Q. S. Jing, J. Chen, P. Bai, J. J. Bai, G. Zhu, Y. J. Su, Z. L. Wang, *Adv. Funct. Mater.* **2015**, *25*, 2166.
[29] Z. M. Wang, J. An, J. H. Nie, J. J. Luo, J. J. Shao, T. Jiang, B. D. Chen, W. Tang, Z. L. Wang, *Adv. Mater.* **2020**, *32*, 2001466.
[30] W. Li, G. Liu, D. Jiang, C. Wang, W. Li, T. Guo, J. Zhao, F. Xi, W. Liu, C. Zhang, *Adv. Mater. Technol.* **2018**, *3*, 1800189.